



Star Formation Efficiency in Nearby Galaxies Revealed with a New CO-to-H₂ Conversion Factor Prescription

Yu-Hsuan Teng¹ , I-Da Chiang² , Karin M. Sandstrom^{1,3} , Jiayi Sun^{4,5,6} , Adam K. Leroy⁷ , Alberto D. Bolatto⁸ , Antonio Usero⁹ , Eve C. Ostriker⁶ , Miguel Querejeta⁹ , J  r  my Chasten  t¹⁰ , Frank Bigiel¹¹ , M  d  ric Boquien¹² , Jakob den Brok¹³ , Yixian Cao¹⁴ , M  lanie Cheval  re^{15,16} , Ryan Chown⁷ , Dario Colombo¹¹ , Cosima Eibensteiner¹¹ , Simon C. O. Glover¹⁵ , Kathryn Grasha^{13,17,18,25} , Jonathan D. Henshaw^{19,20} , Mar  a J. Jim  nez-Donaire^{9,21} , Daizhong Liu¹⁴ , Eric J. Murphy²² , Hsi-An Pan²³ , Sophia K. Stuber²⁰ , and Thomas G. Williams²⁴

¹ Center for Astrophysics and Space Sciences, Department of Physics, University of California San Diego, 9500 Gilman Drive, La Jolla, CA 92093, USA; yuteng@ucsd.edu

² Institute of Astronomy and Astrophysics, Academia Sinica, No. 1, Section 4, Roosevelt Road, Taipei 10617, Taiwan

³ Department of Astronomy & Astrophysics, University of California San Diego, 9500 Gilman Drive, La Jolla, CA 92093, USA

⁴ Department of Physics and Astronomy, McMaster University, 1280 Main Street West, Hamilton, ON, L8S 4M1, Canada

⁵ Canadian Institute for Theoretical Astrophysics (CITA), University of Toronto, 60 St George Street, Toronto, ON, M5S 3H8, Canada

⁶ Department of Astrophysical Sciences, Princeton University, 4 Ivy Lane, Princeton, NJ 08544, USA

⁷ Department of Astronomy, The Ohio State University, 140 West 18th Avenue, Columbus, OH 43210, USA

⁸ Department of Astronomy, University of Maryland, College Park, MD 20742, USA

⁹ Observatorio Astron  mico Nacional (IGN), C/Alfonso XII, 3, E-28014 Madrid, Spain

¹⁰ Sterrenkundig Observatorium, Universiteit Gent, Krijgslaan 281 S9, B-9000 Gent, Belgium

¹¹ Argelander-Institut f  r Astronomie, Universit  t Bonn, Auf dem H  gel 71, D-53121 Bonn, Germany

¹² Instituto de Alta Investigaci  n, Universidad de Tarapac  , Casilla 7D, Arica, Chile

¹³ Center for Astrophysics | Harvard & Smithsonian, 60 Garden Street, Cambridge, MA 02138, USA

¹⁴ Max-Planck-Institut f  r extraterrestrische Physik, Giessenbachstra   1, D-85748 Garching, Germany

¹⁵ Universit  t Heidelberg, Zentrum f  r Astronomie, Institut f  r Theoretische Astrophysik, Albert-Ueberle-Str 2, D-69120 Heidelberg, Germany

¹⁶ Cosmic Origins Of Life (COOL) Research DAO, coolresearch.io, Germany

¹⁷ Research School of Astronomy and Astrophysics, Australian National University, Canberra, ACT 2611, Australia

¹⁸ ARC Centre of Excellence for All Sky Astrophysics in 3 Dimensions (ASTRO 3D), Australia

¹⁹ Astrophysics Research Institute, Liverpool John Moores University, 146 Brownlow Hill, Liverpool, L3 5RF, UK

²⁰ Max-Planck-Institut f  r Astronomie, K  nigstuhl 17, D-69117, Heidelberg, Germany

²¹ Centro de Desarrollos Tecnol  gicos, Observatorio de Yebes (IGN), E-19141 Yebes, Guadalajara, Spain

²² National Radio Astronomy Observatory, 520 Edgemont Road, Charlottesville, VA 22903-2475, USA

²³ Department of Physics, Tamkang University, No.151, Yingzhuan Road, Tamsui District, New Taipei City 251301, Taiwan

²⁴ Sub-department of Astrophysics, Department of Physics, University of Oxford, Keble Road, Oxford, OX1 3RH, UK

Received 2023 October 19; revised 2023 November 22; accepted 2023 November 23; published 2024 January 12

Abstract

Determining how the galactic environment, especially the high gas densities and complex dynamics in bar-fed galaxy centers, alters the star formation efficiency (SFE) of molecular gas is critical to understanding galaxy evolution. However, these same physical or dynamical effects also alter the emissivity properties of CO, leading to variations in the CO-to-H₂ conversion factor (α_{CO}) that impact the assessment of the gas column densities and thus of the SFE. To address such issues, we investigate the dependence of α_{CO} on the local CO velocity dispersion at 150 pc scales using a new set of dust-based α_{CO} measurements and propose a new α_{CO} prescription that accounts for CO emissivity variations across galaxies. Based on this prescription, we estimate the SFE in a sample of 65 galaxies from the PHANGS–Atacama Large Millimeter/submillimeter Array survey. We find increasing SFE toward high-surface-density regions like galaxy centers, while using a constant or metallicity-based α_{CO} results in a more homogeneous SFE throughout the centers and disks. Our prescription further reveals a mean molecular gas depletion time of 700 Myr in the centers of barred galaxies, which is overall three to four times shorter than in nonbarred galaxy centers or the disks. Across the galaxy disks, the depletion time is consistently around 2–3 Gyr, regardless of the choice of α_{CO} prescription. All together, our results suggest that the high level of star formation activity in barred centers is not simply due to an increased amount of molecular gas, but also to an enhanced SFE compared to nonbarred centers or disk regions.

Unified Astronomy Thesaurus concepts: CO line emission (262); Disk galaxies (391); Galaxy nuclei (609); Giant molecular clouds (653); Star formation (1569)

1. Introduction

Star formation in galaxies is governed by the amount of molecular gas and the efficiency with which that gas is converted into stars. To understand the evolutionary process of star formation activity within galaxies, it is critical to measure the molecular gas star formation efficiency (SFE; defined as the ratio between the star formation rate, or SFR, and molecular gas mass, M_{mol}) or the molecular gas depletion time

²⁵ ARC DECRA Fellow.



($t_{\text{dep}} = 1/\text{SFE}$; see the review by Saintonge & Catinella 2022). Previous studies have found that SFR and molecular gas surface densities are highly correlated (i.e., the molecular Kennicutt–Schmidt, or mKS, relation; Kennicutt 1998) and that t_{dep} is usually at 1–4 Gyr across nearby star-forming galaxies (e.g., Bigiel et al. 2008; Leroy et al. 2008; Saintonge et al. 2011; Schruba et al. 2011; Utomo et al. 2017; Sun et al. 2023). Despite the minor variation in general, t_{dep} is also found to vary systematically with local and global host galaxy properties, which could be driven by environmental and/or dynamical effects from, e.g., metallicity, molecular cloud structure, bar instabilities, active galactic nuclei, or galaxy interactions (Saintonge et al. 2011, 2012; Schruba et al. 2019; Ellison et al. 2021a, 2021b; Querejeta et al. 2021; Lu et al. 2022; Villanueva et al. 2022; Jiménez-Donaire et al. 2023; Maeda et al. 2023).

The assessment of molecular gas SFE relies heavily on the CO-to- H_2 conversion factor (α_{CO}).²⁶

$$\alpha_{\text{CO}} = \frac{M_{\text{mol}}}{L'_{\text{CO}(1-0)}} = \frac{\Sigma_{\text{mol}}}{I_{\text{CO}(1-0)}} \left[\frac{M_{\odot}}{\text{K km s}^{-1} \text{pc}^2} \right], \quad (1)$$

where M_{mol} (Σ_{mol}) is the total molecular gas mass (surface density) and $L'_{\text{CO}(1-0)}$ ($I_{\text{CO}(1-0)}$) is the line luminosity (intensity) of CO $J=1-0$. α_{CO} is known to vary with molecular gas conditions such as density, temperature, and dynamical state (see the review by Bolatto et al. 2013, hereafter B13), which are the same conditions that could also alter the intrinsic SFE of the molecular gas. Due to the lack of a widely agreed prescription that can accurately predict α_{CO} , many studies could only assume a constant α_{CO} referencing the Milky Way (MW) disk average (e.g., B13) to convert CO observations to molecular gas mass. This has made α_{CO} variation one of the dominant sources of uncertainty in current molecular gas and SFE studies (see the discussions in Ellison et al. 2020b; Maeda et al. 2023; Sun et al. 2023).

The impacts of α_{CO} variations on both SFE and cloud evolutionary timescale estimates are particularly critical in galaxy centers (Leroy et al. 2013; Utomo et al. 2017; Muraoka et al. 2019; Ellison et al. 2020b; Pessa et al. 2021; Maeda et al. 2023; Sun et al. 2023). In those environments, α_{CO} can be 5–15 times lower than the Galactic disk value (Ackermann et al. 2012; Sandstrom et al. 2013; Israel 2020; Teng et al. 2022, 2023; den Brok et al. 2023). The lower α_{CO} in galaxy centers is likely driven by CO emissivity variations due to higher excitation and/or stronger dynamical effects, such as turbulence or inflowing gas (Narayanan et al. 2012; Papadopoulos et al. 2012; B13; Gong et al. 2020; Teng et al. 2023). These effects may also explain the low α_{CO} seen in mergers or (ultra)luminous infrared galaxies (U/LIRGs; Downes & Solomon 1998; Krieger et al. 2017; Sliwa et al. 2017; Cicone et al. 2018; Herrero-Illana et al. 2019).

Reducing the uncertainty in molecular gas and SFE studies, and thereby improving our understanding of star formation and galaxy evolution, requires a robust α_{CO} prescription that can be systematically applied to large samples of galaxies with diverse environments. Recent studies have proposed various types of α_{CO} prescription, depending on metallicity, stellar mass surface

density, SFR, SFE, and/or CO line-related properties (Genzel et al. 2012; Narayanan et al. 2012; B13; Hunt et al. 2015; Amorín et al. 2016; Accurso et al. 2017; Renaud et al. 2019; Gong et al. 2020; Madden et al. 2020; Ramambason et al. 2023). However, establishing a reliable α_{CO} calibration remains a challenge, because it requires α_{CO} measurements covering a sufficient sample of galaxies spanning a broad range of molecular gas physical and dynamical conditions, and the two most realistic ways to measure α_{CO} in nearby galaxies are via dust emission (which is typically restricted to kiloparsec resolutions; Israel 1997; Leroy et al. 2011; Sandstrom et al. 2013; Schruba et al. 2017; Pitts & Barnes 2021; Chiang et al. 2023; den Brok et al. 2023; Yasuda et al. 2023) or multi-CO isotopologue observations (which are expensive at cloud scales; Sliwa et al. 2017; Cormier et al. 2018; Israel 2020; Sharda et al. 2022; Teng et al. 2022, 2023).

Thanks to the high resolution and sensitivity of the Atacama Large Millimeter/submillimeter Array (ALMA), CO (isotopologue) observations are now routinely possible at cloud scales in nearby galaxies (e.g., Leroy et al. 2021; Davis et al. 2022; Koda et al. 2023; Williams et al. 2023). In particular, recent studies modeling multi-CO isotopologues in nearby galaxy centers have revealed that CO opacity is the dominant driver of α_{CO} variations (Israel 2020; Teng et al. 2022, 2023). This strong dependence of α_{CO} on CO opacity further leads to a clear anticorrelation between α_{CO} and the observed line width at ~ 100 pc scales in barred galaxy centers (Teng et al. 2023, hereafter T23).

Motivated by these latest measurements of α_{CO} , we will test if the correlation found in T23 also applies to the 12 galaxies (labeled with * in Table 1; including eight barred and four nonbarred) that have dust-inferred α_{CO} values at kiloparsec scales (from Chiang et al. 2023, hereafter C23) and molecular gas velocity dispersion measured at 150 pc scales (from the PHANGS–ALMA survey; Leroy et al. 2021; Sun et al. 2022). The results of this comparison lead us to a new α_{CO} prescription capturing CO emissivity effects in star-forming galaxies. In this paper, we present this prescription, discuss its physical implications, and study its impact on SFE across a sizable sample of galaxy centers and disks with diverse properties.

2. Data and Measurements

2.1. PHANGS Data Sets

Our analysis is based on various molecular gas and star formation properties, leveraging a database developed by Sun et al. (2022) that assembled multiwavelength measurements of 80 galaxies from the PHANGS–ALMA survey (Leroy et al. 2021). From this database, we extract multiple physical quantities in matched hexagonal apertures with fixed sizes of 1.5 kpc. The quantities used in this work include: the intensity-weighted mean molecular gas velocity dispersion measured at 150 pc scale ($\langle \Delta v \rangle_{150 \text{ pc}}$), the area-weighted mean CO(2–1) line integrated intensity ($I_{\text{CO}(2-1)}$), the stellar mass surface density (Σ_{star}), the SFR surface density (Σ_{SFR}), and the gas-phase metallicity (Z' , normalized to the solar value [$12 + \log(\text{O}/\text{H})_{\odot} = 8.69$] and calibrated based on Pettini & Pagel 2004). All these quantities are corrected for the effects of galaxy inclination and data sensitivity limits (see Sun et al. 2022 for more details).

²⁶ α_{CO} is defined for the CO $J=1-0$ line in most literature, but it can also be evaluated for other transitions. In this work, when we refer to α_{CO} , we mean $\alpha_{\text{CO}(1-0)}$ unless otherwise specified.

Table 1
Galaxy Sample and Properties in the Central 1.5 kpc Regions

Galaxy	Bar	Dist.	Incl.	P.A.	Z'	$\log(\Sigma_{\text{SFR}})$	$I_{\text{CO}(2-1)}$	$\log(\Sigma_{\text{star}})$	$\langle \Delta v \rangle_{150 \text{ pc}}$	$\log(\alpha_{\text{CO}}^{\text{Equation 2}})$	$\log(t_{\text{dep}})$
(1)	(2)	(Mpc) (3)	(deg) (4)	(deg) (5)	(Z_{\odot}) (6)	($\frac{M_{\odot}}{\text{yr kpc}^2}$) (7)	(K km s $^{-1}$) (8)	($M_{\odot} \text{ pc}^{-2}$) (9)	(km s $^{-1}$) (10)	($\frac{M_{\odot} \text{ s}}{\text{K km pc}^2}$) (11)	(yr) (12)
IC1954	1	12.8	57.1	63.4	1.10	−1.67	7.5	2.51	7.1	0.36	9.08
IC5273	1	14.2	52.0	234.1	1.12	−1.59	4.7	2.48	7.4	0.34	8.78
NGC0253*	1	3.7	75.0	52.5	1.33	0.3166	198.2	990.2	28.5	−0.15	8.88
NGC0628*	0	9.8	8.9	20.7	1.29	−1.82	6.3	3.03	5.4	0.45	9.26
NGC0685	1	19.9	23.0	100.9	1.23	−2.15	2.8	2.42	6.8	0.37	9.15
NGC1087	1	15.8	42.9	359.1	1.19	−1.12	24.7	2.68	13.4	0.12	8.82
NGC1097	1	13.6	48.6	122.4	1.34	−0.29	196.0	3.61	33.1	−0.20	8.57
NGC1300	1	19.0	31.8	278.0	1.33	−1.57	44.6	3.25	23.2	−0.07	9.33
NGC1317	1	19.1	23.2	221.5	1.33	−1.45	25.2	3.64	18.0	0.02	9.06
NGC1365	1	19.6	55.4	201.1	1.36	0.04	462.4	3.80	25.6	−0.11	8.70
NGC1385	0	17.2	44.0	181.3	1.21	−1.00	15.0	2.78	9.5	0.25	8.60
NGC1433	1	18.6	28.6	199.7	1.35	−1.46	44.6	3.63	17.3	0.03	9.33
NGC1511	0	15.3	72.7	297.0	1.18	−1.17	12.4	2.60	7.5	0.33	8.79
NGC1512	1	18.8	42.5	261.9	1.34	−1.36	31.9	3.41	11.3	0.19	9.24
NGC1546	0	17.7	70.3	147.8	1.29	−1.52	45.0	3.08	7.9	0.31	9.67
NGC1559	1	19.4	65.4	244.5	1.29	−1.47	10.5	2.77	6.6	0.38	9.06
NGC1566	1	17.7	29.5	214.7	1.34	−0.97	55.7	3.63	28.7	−0.15	8.76
NGC1637	1	11.7	31.1	20.6	1.20	−0.82	12.2	2.57	22.8	−0.07	8.03
NGC1792	0	16.2	65.1	318.9	1.33	−1.35	52.0	3.08	10.7	0.21	9.46
NGC1809	0	20.0	57.6	138.2	1.14	−1.71	2.2	2.19	3.1	0.65	8.88
NGC2090	0	11.8	64.5	192.5	1.22	−2.19	4.5	2.79	4.2	0.54	9.57
NGC2283	1	13.7	43.7	−4.1	1.18	−1.93	3.0	2.31	5.1	0.47	9.07
NGC2566	1	23.4	48.5	312.0	1.34	−0.05	265.0	3.16	26.5	−0.12	8.53
NGC2835	1	12.2	41.3	1.0	1.21	−2.23	2.2	2.47	4.3	0.53	9.30
NGC2903	1	10.0	66.8	203.7	1.33	−0.81	55.8	3.15	19.7	−0.01	8.73
NGC2997	0	14.1	33.0	108.1	1.34	−0.95	68.5	3.21	16.2	0.06	9.03
NGC3059	1	20.2	29.4	−14.8	1.29	−0.84	23.1	2.68	11.4	0.18	8.58
NGC3137	0	16.4	70.3	−0.3	1.18	−2.53	3.0	2.19	3.2	0.64	9.85
NGC3351*	1	10.0	45.1	193.2	1.29	−0.71	34.4	3.18	19.2	−0.01	8.43
NGC3507	1	23.6	21.7	55.8	1.30	−1.57	17.3	3.16	23.4	−0.08	8.91
NGC3511	1	13.9	75.1	256.8	1.22	−1.94	17.2	2.50	6.6	0.38	9.74
NGC3521*	0	13.2	68.8	343.0	1.36	−1.66	14.8	3.50	6.7	0.37	9.40
NGC3596	0	11.3	25.1	78.4	1.10	−1.55	6.3	2.68	7.0	0.36	8.90
NGC3621	0	7.1	65.8	343.8	1.23	−1.86	8.4	2.66	5.2	0.46	9.44
NGC3626	1	20.0	46.6	165.2	1.31	−1.40	11.2	3.52	13.5	0.12	8.76
NGC3627*	1	11.3	57.3	173.1	1.35	−1.19	64.9	3.53	34.6	−0.22	8.98
NGC4254*	0	13.1	34.4	68.1	1.30	−1.10	35.7	3.27	10.3	0.22	9.06
NGC4293	1	15.8	65.0	48.3	1.31	−1.11	45.0	2.92	27.4	−0.13	8.82
NGC4298	0	14.9	59.2	313.9	1.22	−1.79	14.3	2.69	9.7	0.24	9.38
NGC4303	1	17.0	23.5	312.4	1.32	−0.83	70.8	3.52	16.9	0.04	8.91
NGC4321*	1	15.2	38.5	156.2	1.34	−0.78	101.0	3.35	19.5	−0.01	8.96
NGC4457	1	15.1	17.4	78.7	1.30	−1.15	38.7	3.69	29.0	−0.15	8.77
NGC4496A	1	14.9	53.8	51.1	1.04	−2.21	1.6	2.17	2.8	0.69	9.29
NGC4535	1	15.8	44.7	179.7	1.32	−1.03	43.1	2.78	20.1	−0.02	8.83
NGC4536*	1	16.2	66.0	305.6	1.30	−0.56	110.3	3.30	21.0	−0.04	8.76
NGC4540	1	15.8	28.7	12.8	1.14	−1.90	3.9	2.65	6.3	0.40	9.07
NGC4548	1	16.2	38.3	138.0	1.34	−1.96	9.7	3.38	24.8	−0.10	9.03
NGC4569*	1	15.8	70.0	18.0	1.35	−1.13	112.1	3.24	27.6	−0.14	9.23
NGC4571	0	14.9	32.7	217.5	1.23	−2.36	2.5	2.63	2.7	0.70	9.63
NGC4689*	0	15.0	38.7	164.1	1.26	−1.81	9.2	2.61	5.6	0.44	9.40
NGC4731	1	13.3	64.0	255.4	1.02	−1.97	1.6	1.99	5.1	0.47	8.85
NGC4781	1	11.3	59.0	290.0	1.09	−1.76	9.1	2.59	8.2	0.30	9.20
NGC4826	0	4.4	59.1	293.6	1.27	−1.43	27.9	3.26	21.8	−0.05	9.01
NGC4941*	1	15.0	53.4	202.2	1.25	−1.31	6.9	3.00	18.7	0.00	8.34
NGC4951	0	15.0	70.2	91.2	1.15	−1.77	10.0	2.67	11.4	0.18	9.14
NGC5042	0	16.8	49.4	190.6	1.18	−2.15	2.2	2.52	5.3	0.46	9.14
NGC5068	1	5.2	35.7	342.4	0.98	−2.01	1.0	2.33	3.6	0.60	8.79
NGC5128	0	3.7	45.3	32.2	1.36	−0.78	45.3	3.70	22.7	−0.07	8.56
NGC5134	1	19.9	22.7	311.6	1.30	−1.94	4.9	3.33	11.4	0.18	9.00
NGC5248*	1	14.9	47.4	109.2	1.30	−0.97	72.6	3.35	15.7	0.07	9.08
NGC5530	0	12.3	61.9	305.4	1.23	−2.02	6.4	3.00	4.8	0.50	9.51
NGC5643	1	12.7	29.9	318.7	1.29	−0.29	42.0	2.88	26.7	−0.12	7.98

Table 1
(Continued)

Galaxy	Bar	Dist.	Incl.	P.A.	Z'	$\log(\Sigma_{\text{SFR}})$	$I_{\text{CO}(2-1)}$	$\log(\Sigma_{\text{star}})$	$\langle \Delta v \rangle_{150 \text{ pc}}$	$\log(\alpha_{\text{CO}}^{\text{Equation 2}})$	$\log(t_{\text{dep}})$
(1)	(2)	(Mpc) (3)	(deg) (4)	(deg) (5)	(Z_{\odot}) (6)	($\frac{M_{\odot}}{\text{yr kpc}^2}$) (7)	(K km s^{-1}) (8)	($M_{\odot} \text{ pc}^{-2}$) (9)	(km s^{-1}) (10)	($\frac{M_{\odot} \text{ s}}{\text{K km pc}^2}$) (11)	(yr) (12)
NGC6300	1	11.6	49.6	105.4	1.31	-0.55	41.1	2.85	36.2	-0.23	8.11
NGC7456	0	15.7	67.3	16.0	1.09	-2.70	0.9	1.99	2.7	0.70	9.56
NGC7496	1	18.7	35.9	193.7	1.21	-0.43	46.2	2.72	23.7	-0.08	8.20

Note. Column (1): the galaxies with an asterisk are those with α_{CO} measurements (see Section 2.2). Column (2): bar classification (Querejeta et al. 2021). Column (3): distance (Anand et al. 2021). Columns (4)–(5): inclination and position angles (Lang et al. 2020). Columns (6)–(10): the central 1.5 kpc measurements of gas-phase metallicity (PP04-based), kiloparsec-averaged SFR surface density, kiloparsec-averaged CO(2–1) integrated intensity, kiloparsec-averaged stellar mass surface density, and CO intensity-weighted mean velocity dispersion at 150 pc scale (Sun et al. 2022). Column (11): $\log(\alpha_{\text{CO}})$ derived from Column (10) using Equation (2). Column (12): molecular gas depletion time derived from Columns (7), (8), and (11) using Equation (6).

To further explore trends in galaxies with or without stellar bars, we adopt the classification of stellar bars for PHANGS galaxies (Querejeta et al. 2021). Table 1 lists the 65 galaxies included in our analysis, which is the overlap between Querejeta et al. (2021) and Sun et al. (2022). This sample from PHANGS has high-resolution CO(2–1) data with beam sizes of 150 pc or smaller. Columns (6)–(10) in Table 1 show the measurements extracted from Sun et al. (2022) for the central 1.5 kpc regions of those galaxies.

2.2. Dust-based α_{CO} Measurements

We obtain spatially resolved α_{CO} from C23, where α_{CO} is measured at 2 kpc resolution across 41 nearby (≤ 20 Mpc) and moderately inclined (Incl. $\leq 80^\circ$) spiral galaxies with resolved measurements of CO integrated intensity (including PHANGS–ALMA) and atomic gas. The authors assumed a constant dust-to-metals ratio to constrain the total gas mass with dust and metallicity measurements. In their sample, eight barred and four nonbarred galaxies from PHANGS have dust-based α_{CO} measurements (those with an * in Table 1). These measurements typically cover out to a galactocentric radius of ~ 10 kpc, including ~ 2000 Nyquist-sampled data points. It is based on these data that we examine the scaling relations of α_{CO} and develop an α_{CO} prescription in Section 3.1.

The α_{CO} measurements in C23 were derived based on the PHANGS CO(2–1) data, and we directly use their $\alpha_{\text{CO}(2-1)}$ measurements to ensure methodological consistency when we derive the molecular gas surface density and SFE (see Sections 3.3 and 3.4). To compare with most α_{CO} literature using $\alpha_{\text{CO}(1-0)}$, however, we convert the measured $\alpha_{\text{CO}(2-1)}$ to $\alpha_{\text{CO}(1-0)}$ by assuming a CO(2–1)/(1–0) ratio (R_{21}) of 0.65. Such results can be easily reverted to $\alpha_{\text{CO}(2-1)}$ via a linear scaling with 0.65. We note that C23 also provided $\alpha_{\text{CO}(1-0)}$ measurements assuming an SFR-dependent R_{21} , and we have checked that using such α_{CO} does not change any of our results qualitatively (see Section 3.1).

We also note that the metallicity adopted by C23 for computing α_{CO} is based on the S-calibration in Pilyugin & Grebel (2016, hereafter PG16S), which is different from the O3N2 calibration used for the PHANGS data set based on Pettini & Pagel (2004, hereafter PP04). Recent studies suggest that PG16S is a more reliable metallicity prescription than PP04 (e.g., Kreckel et al. 2019). With the data on 12 galaxies, we find that PP04 estimates result in ~ 0.2 dex higher Z' than PG16S (see also De Vis et al. 2019), which might be due to the mismatch in the adopted solar oxygen abundance

value under different calibration schemes (e.g., $12 + \log(\text{O}/\text{H})_{\odot} = 8.50$ or 8.69 ; see the discussion in Esteban et al. 2022). Throughout this work, we adopt PG16S-based Z' from C23 for analyses restricted to these 12 galaxies. However, due to the lack of PG16S-based measurements on all 65 PHANGS galaxies, we use the PP04-based Z' when implementing metallicity-dependent α_{CO} prescriptions across the full sample for consistency.

To evaluate the credibility of the observed α_{CO} trends with our parameters of interest (i.e., $\langle \Delta v \rangle_{150 \text{ pc}}$ and Z'), we calculate for each parameter bin the number of pixels with reliable α_{CO} measurements divided by the number of pixels with measured Δv or Z' . For Δv , we find the fraction of reliable pixels to be 70%–100% for bins with $\langle \Delta v \rangle_{150 \text{ pc}} \gtrsim 3 \text{ km s}^{-1}$, while it drops significantly to $< 50\%$ in lower-velocity-dispersion bins.²⁷ This means that our α_{CO} data coverage is insufficient to accurately represent regions with $\Delta v \lesssim 3 \text{ km s}^{-1}$. As for Z' , the corresponding completeness of α_{CO} is above 60% across regions with $Z' \gtrsim 0.6$, while it drops below 40% at lower metallicities (where the PHANGS–ALMA data set has poorer coverage). These “incomplete” regimes will be excluded by our fitting and analysis in Section 3.1, where we present the new α_{CO} prescription.

3. Results

3.1. A Velocity-dispersion-based α_{CO} Prescription

To investigate how the dust-based α_{CO} varies with local velocity dispersion, we use nearest-neighbor matching to relate the α_{CO} measurements at 2 kpc scales with the velocity dispersion that is measured at 150 pc scale and then averaged over 1.5 kpc sized apertures via intensity weighting ($\langle \Delta v \rangle_{150 \text{ pc}}$). As shown in Figure 1(a), the data clearly follow an inverse power-law relation, which is in close agreement with the fit by T23 on three barred galaxy centers at ~ 100 pc scales (i.e., the dashed-dotted orange line, assuming a CO/H₂ abundance of 1.5×10^{-4}). The central regions of the 12 galaxies (the vertical gray bars in Figure 1(a)) align well with the overall trend, showing that velocity dispersion can trace α_{CO} variations in both the centers and disks.²⁸ The green cross sign marks the typical MW disk values of $\alpha_{\text{CO}} \sim 4.35 M_{\odot} (\text{K km s}^{-1} \text{ pc}^2)^{-1}$ and $\Delta v = 5 \text{ km s}^{-1}$, which also agrees

²⁷ This is likely due to a large amount of low-signal-to-noise-ratio measurements clustering around $\sim 2.5 \text{ km s}^{-1}$, which is the velocity resolution of the PHANGS CO data.

²⁸ In this paper, “center” refers to the central ~ 2 kpc sized aperture at $R_{\text{gal}} = 0$, and “disks” represents the rest of the measurements.

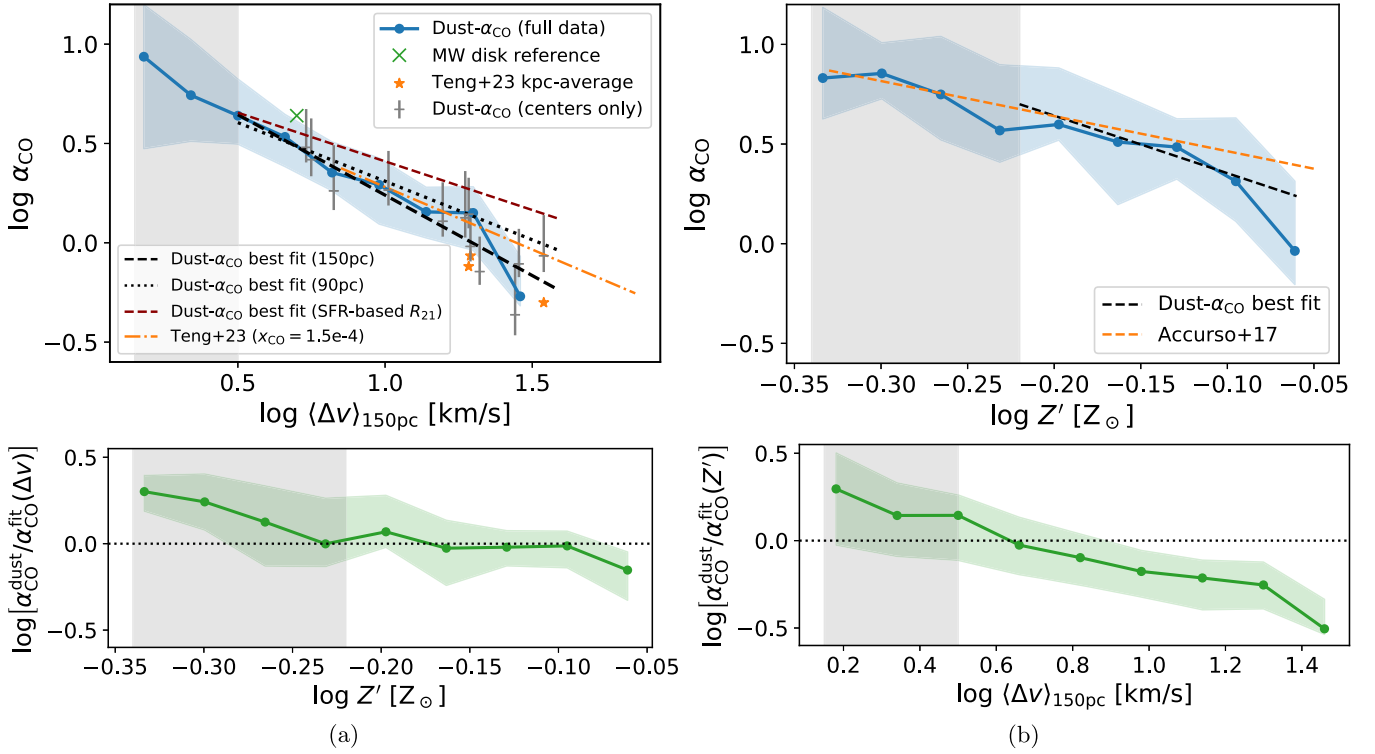


Figure 1. (a) Dust-based α_{CO} measurements show a strong anticorrelation with the intensity-weighted average of 150 pc scale molecular gas velocity dispersion (top), consistent with the result from T23 on barred galaxy centers (orange line, with an assumed CO/H_2 abundance $x_{\text{CO}} = 1.5 \times 10^{-4}$); the blue lines and shaded area represent the binned medians and 16th–84th percentiles of the measured α_{CO} ; the gray shaded area indicates the low-confidence regime where α_{CO} sampling is incomplete; the black dashed-dotted lines show the best-fit power-law relations with $\langle \Delta v \rangle$ at 150/90 pc resolutions; and the red dashed line represents the best-fit relation when α_{CO} is derived by assuming an SFR-dependent R_{21} (C23). The residuals of the fit (bottom) do not correlate with Z' in the data-complete regime, suggesting that the observed α_{CO} variations can be fully captured by our Δv -based prescription, without requiring an additional metallicity dependence. (b) Similar to (a), but the measured α_{CO} is correlated with metallicity (top), and the residuals are correlated with $\langle \Delta v \rangle_{150\text{pc}}$ (bottom); the orange dashed line marks the prediction from Accurso et al. (2017), which agrees with the overall data but shows a larger scatter.

with the overall trend. The shaded area in Figure 1(a) indicates the regime where α_{CO} data are incomplete (see Section 2.2).

Excluding the incomplete regime, we conduct a least-squares fitting in log-log space based on the remaining ~ 1600 data points, using the `curve_fit` function in `scipy.optimize`. The best-fit power-law relation to these data from 12 galaxies is represented by

$$\log \alpha_{\text{CO}} = -0.81 \log \langle \Delta v \rangle_{150\text{pc}} + 1.05, \quad (2)$$

where α_{CO} and $\langle \Delta v \rangle_{150\text{pc}}$ are in units of $M_{\odot} (\text{K km s}^{-1} \text{pc}^2)^{-1}$ and km s^{-1} , respectively. The best-fit relation is shown by the black dashed line in the top panel of Figure 1(a) and is consistent with the trend of the binned α_{CO} medians. The dispersion of data with respect to Equation (2) is $\sigma \sim 0.12$ dex, and the standard deviation error returned by `curve_fit` is ± 0.02 for both the fitted slope and intercept. We remind readers that the α_{CO} data here are converted from $\alpha_{\text{CO}(2-1)}$ assuming $R_{21} = 0.65$, and thus should be scaled by $R_{21}/0.65$ if R_{21} is known. If an SFR-dependent R_{21} is used, following C23, the trend of α_{CO} in Figure 1(a) could be shallower by 30%–40%, as indicated by the red dashed line.

While the functional fit in Equation (2) is based on Δv measured at 150 pc scale, we also find a similar best-fit relation (dotted line) for six of those galaxies where $\langle \Delta v \rangle_{90\text{pc}}$ is available. Because Δv does not vary strongly between 90 and 150 pc scales (see also Sun et al. 2022), we would not expect this to change our results, and thus Equation (2) should be applicable with Δv measurements around 100 pc resolutions.

We note that the evaluation of Δv can also be affected by the number of gas components overlapping along the same sightlines, which could increase Δv in barred galaxy centers. However, such an effect is found to be mild (see T23, Appendix A), and we expect it to be even milder in our case, as $\langle \Delta v \rangle_{150\text{pc}}$ is averaged over kiloparsec-sized regions.

3.2. Comparison to Previous Literature

We compare our Δv -based prescription with existing α_{CO} prescriptions in the literature, including those based on metallicity (Accurso et al. 2017; Sun et al. 2020a) or combining metallicity and stellar mass surface density (B13). First, we investigate if metallicity alone could trace the observed α_{CO} variations. Figure 1(b) relates the measured α_{CO} with metallicity, using the same metallicity as those used in C23 to calculate α_{CO} (see Section 2.2). The data and the power-law fit (black dashed line) overall agree with the purely metallicity-dependent α_{CO} prescription from Accurso et al. (2017; orange dashed line),²⁹ although the data scatter is larger than the trend with velocity dispersion. In the regime where our data set is complete, the scatter of the observed α_{CO} is $\sigma \sim 0.1$ dex with $\langle \Delta v \rangle_{150\text{pc}}$ and 0.3 dex with Z' . This shows a significant improvement in predicting α_{CO} with our Δv -based prescription, compared to current metallicity-dependent prescriptions.

²⁹ The Z' in the original prescription [$\alpha_{\text{CO}} = 4.35(Z')^{-1.6}$] was based on the PP04 calibration. Here we convert their prescription to the same (PG16S-based) metallicity scale as we adopt, using an approximate conversion based on De Vis et al. (2019).

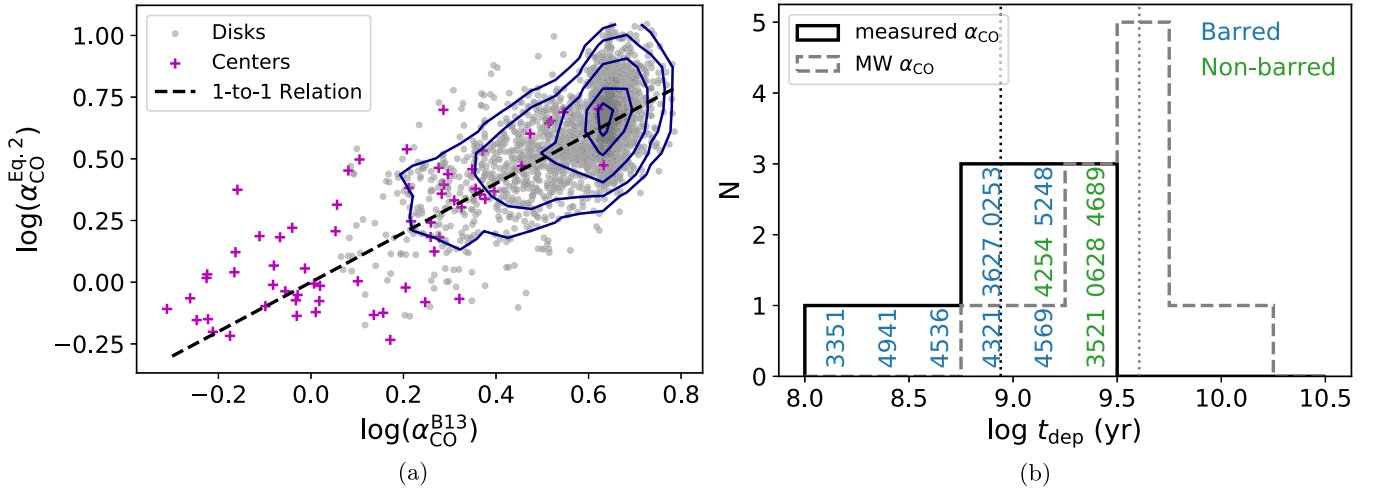


Figure 2. (a) Comparison of the derived α_{CO} using our Δv -based prescription (Equation (2)) and the Z' plus Σ_{star} -based prescription (Equation (3); B13), applied to 65 galaxies. The overlaid contours indicate 16%, 50%, 84%, 95%, and 98% data inclusion of the disk regions. The two prescriptions show a general one-to-one agreement (dashed line), which supports the credibility of our prescription. (b) Molecular gas depletion time (t_{dep}) of 12 galaxy centers (with their NGC names shown on the histogram) determined by the measured α_{CO} (solid line) and the MW α_{CO} (dashed line). The median t_{dep} using measured or MW α_{CO} are indicated by the vertical dotted lines. Overall, t_{dep} is lower using the measured α_{CO} , and a clear separation is found between barred and nonbarred galaxies, suggesting high SFE in barred galaxy centers.

In the bottom panels of Figures 1(a) and (b), we relate the residuals of each α_{CO} fit with Z' or $\langle \Delta v \rangle_{150 \text{ pc}}$, in order to check if metallicity effects can explain any residual variation of α_{CO} around the Δv trend, or the opposite. Above the completeness limit, we find no trend between the residuals from the Δv prescription and metallicity. On the other hand, the residuals from the metallicity fit clearly decrease with Δv above the completeness threshold. This suggests that Δv is crucial for tracing the α_{CO} changes, even without including metallicity effects. We have checked that the α_{CO} correlation with Z' seen in this regime may come from the correlation between Z' and Δv , as both variables decrease with the galactocentric radius.

Taking both metallicity and emissivity effects into account, B13 also suggested a tentative prescription³⁰ based on α_{CO} measurements in nearby disks and (U)LIRGs:

$$\alpha_{\text{CO}} \approx 2.9 \exp\left(\frac{0.4}{Z'}\right) \left(\frac{\Sigma_{\text{star}} + \Sigma_{\text{mol}}}{100 M_{\odot} \text{pc}^{-2}}\right)^{-\gamma}, \quad (3)$$

where $\gamma = 0.5$ if $\Sigma_{\text{star}} + \Sigma_{\text{mol}} > 100 M_{\odot} \text{pc}^{-2}$ or $\gamma = 0$ otherwise. To compare the derived α_{CO} from our proposed prescription (Equation (2)) with that from B13, we apply both prescriptions to galaxies in the PHANGS sample (see Table 1) using kiloparsec-scale Z' and Σ_{star} . As we find $\Sigma_{\text{mol}} \ll \Sigma_{\text{star}}$ even with a (likely overestimated) Galactic α_{CO} (Sun et al. 2022), we neglect Σ_{mol} in Equation (3). We note that C23 also reported a similar α_{CO} relation that scales with $\Sigma_{\text{star}}^{-0.5}$.

Figure 2(a) compares the α_{CO} values predicted by Equations (2) and (3). Excluding the regime of $\log(\alpha_{\text{CO}}) \gtrsim 0.65$, where B13 enforces an MW-like α_{CO} value with $\gamma = 0$ (which also corresponds to the low-confidence regime of our Δv -based prescription), the two prescriptions show an overall match with a ~ 0.5 dex scatter. Despite a significant scatter, this general agreement may indicate that Δv and Σ_{star} are tracing the same physical process that drives α_{CO}

variations. A likely scenario is that Δv is set by the additional gravitational potential from stellar components, which can thus be tracked by Σ_{star} (see B13 and C23). It is also possible that Δv is a proxy of molecular gas surface densities and/or local CO intensities that could also reflect opacity and α_{CO} changes, as previous studies have found good correlations between these properties (Sun et al. 2022; see also Section 4 for further discussion).

The B13 prescription was mostly based on α_{CO} measurements that were independent from ours and included several U/LIRGs in their sample, and the ~ 0.5 dex scatter with our prescription is also consistent with the uncertainty estimated by B13. Therefore, the rough agreement seen in Figure 2(a) may also provide additional evidence for the validity of our proposed prescription. Compared to a Σ_{star} -based prescription, one advantage of using a Δv -based prescription is that Δv straightforwardly traces the optical depth change (Teng et al. 2022, T23), making it closer to the underlying physics that could control α_{CO} variations. Another advantage is that Δv can be directly obtained from the CO data. Thus, no ancillary multiband data are needed to estimate α_{CO} , which circumvents uncertainties in translating observations into Σ_{star} . We remind readers that our prescription is calibrated to $\langle \Delta v \rangle_{150 \text{ pc}}$ in CO(2–1), which is typically consistent with $\langle \Delta v \rangle_{150 \text{ pc}}$ in CO(1–0), but may be different from that measured in higher- J CO lines (Yuan et al. 2020; Teng et al. 2022, T23). We also point out that systematic measurements of Δv at 150 pc resolutions can be difficult across more extreme starbursts like U/LIRGs (e.g., Wilson et al. 2019), which are usually more distant and/or more morphologically disturbed than the galaxies in our sample.

We note that the scaling of α_{CO} with Δv in Equation (2) is similar to what would be predicted by simple theoretical arguments. As shown by Equation (8) in Gong et al. (2020; see also the related derivations in Chapter 19 of Draine 2011 and Chapter 8 of Krumholz 2015), the excitation temperature (T_{ex}) under a large velocity gradient approximation with assumptions

³⁰ The original prescription included a molecular cloud surface density term that was assumed at $100 M_{\odot} \text{pc}^{-2}$. Here we adopt the same value and note that this helps avoid unrealistic α_{CO} values in low-surface-density regions (Sun et al. 2023; T23).

of a two-level optically thick system can be written as

$$T_{\text{ex}} \propto \rho_{\text{mol}} \sqrt{\frac{L_{\text{mol}} \cdot x_{\text{CO}}}{\Delta v}}, \quad (4)$$

where ρ_{mol} and L_{mol} are the density and size of a CO-emitting molecular cloud, respectively. To first order, we also have $I_{\text{CO}} \sim T_{\text{ex}} \cdot \Delta v$ from the cloud. Thus, combining Equation (1) with Equation (4), we obtain

$$\alpha_{\text{CO}} = \frac{\Sigma_{\text{mol}}}{I_{\text{CO}}} \sim \frac{\rho_{\text{mol}} \cdot L_{\text{mol}}}{T_{\text{ex}} \cdot \Delta v} \propto \sqrt{\frac{L_{\text{mol}}}{x_{\text{CO}} \cdot \Delta v}}. \quad (5)$$

The resulting α_{CO} dependence on the inverse square root of Δv is similar to the fits in Figure 1. While the fitted slope for $\langle \Delta v \rangle_{150 \text{ pc}}$ (Equation (2)) is slightly steeper than -0.5 , we emphasize that the above calculation is highly simplified and is only for providing an intuitive check with theoretical expectations.

3.3. SFE in Galaxy Centers

As α_{CO} determines the total molecular gas surface density (Σ_{mol} , in units of $M_{\odot} \text{ pc}^{-2}$), the variation of α_{CO} directly affects the estimation of the molecular gas depletion time (t_{dep}) or SFE ($=1/t_{\text{dep}}$):

$$t_{\text{dep}} = \Sigma_{\text{mol}} / \Sigma_{\text{SFR}} = \alpha_{\text{CO}} \cdot I_{\text{CO}} / \Sigma_{\text{SFR}}. \quad (6)$$

While we examine only the SFE in this work, we note that the impact of α_{CO} on estimating the SFE per molecular cloud freefall time is even more significant, as α_{CO} also affects the assessment of cloud density, which changes the freefall time (e.g., Querejeta et al. 2023; Sun et al. 2023). Motivated by the clear trend of galaxy centers having lower α_{CO} values (Figures 1(a) and 2(a)), we derive t_{dep} for the 12 galaxy centers with α_{CO} measurements (C23; T23) using kiloparsec-scale Σ_{SFR} and $I_{\text{CO}(2-1)}$ (see Table 1). Then we examine how t_{dep} in galaxy centers derived from the measured α_{CO} would differ from that using the standard MW α_{CO} of 4.35 (or 6.7 in terms of $\alpha_{\text{CO}(2-1)} M_{\odot} (\text{K km s}^{-1} \text{ pc}^2)^{-1}$).

Figure 2(b) presents histograms of t_{dep} for the 12 galaxy centers. For the histogram using the measured α_{CO} , we separate barred and nonbarred galaxies with different colors. We find that the median t_{dep} with the MW α_{CO} is 4–5 times longer than that with the measured α_{CO} . Furthermore, adopting the MW α_{CO} results in a similar t_{dep} of ~ 3 Gyr between barred and nonbarred centers. In contrast, if the measured α_{CO} is used, the median t_{dep} of the barred and nonbarred centers becomes 0.6 and 2.0 Gyr, respectively, differing by more than a factor of 3. This suggests that SFE in barred galaxy centers tend to be higher than nonbarred galaxy centers and that using a constant α_{CO} can obscure such a trend.

3.4. Systematic Impact on SFE

With the PHANGS sample (Table 1), we investigate the impact of different α_{CO} prescriptions on SFE or t_{dep} in the centers and disks of barred and nonbarred galaxies. Figure 3 shows the mKS relation across all 65 galaxies measured at the 1.5 kpc scale, comparing Σ_{mol} determined from our α_{CO} prescription (Equation (2)) with that determined using a MW α_{CO} . It is clear that adopting the MW α_{CO} results in a wider range of Σ_{mol} , with values reaching $>1000 M_{\odot} \text{ pc}^{-2}$ in

galaxy centers, while our prescription suggests $\Sigma_{\text{mol}} < 200 M_{\odot} \text{ pc}^{-2}$ in general. Furthermore, our prescription reveals a trend of higher SFE toward higher Σ_{mol} , which steepens the mKS relation for galaxy centers and other high- Σ_{mol} regions. With the MW α_{CO} , however, both galaxy centers and disks exhibit a roughly constant SFE. These results show that α_{CO} and Σ_{mol} in galaxy centers may overall be overestimated by a factor of 5 with the MW α_{CO} , and that the choice of α_{CO} greatly affects our understanding of galactic-scale star formation.

Figure 4 presents histograms of velocity dispersion and t_{dep} across the PHANGS sample, separating centers (upper panels) and disks (lower panels) for barred (blue) and nonbarred (green) galaxies. In nonbarred galaxy centers, $\langle \Delta v \rangle_{150 \text{ pc}}$ is typically $<10 \text{ km s}^{-1}$, while barred centers span a significantly wider range up to $\sim 40 \text{ km s}^{-1}$. On the other hand, barred and nonbarred disks show consistent velocity dispersion, with $\langle \Delta v \rangle_{150 \text{ pc}}$ typically below 5 km s^{-1} , but reaching up to 10 km s^{-1} . These distributions agree with Sun et al. (2020b), who reported similar Δv between galaxy disks and nonbarred centers, but an overall \sim five times higher Δv in barred centers.

We then examine the distribution of t_{dep} derived with different α_{CO} prescriptions. Using our Δv -based prescription, we find distinctly different t_{dep} between barred and nonbarred centers, with the mean/median of t_{dep} in barred galaxy centers (~ 700 Myr) being three times shorter than in nonbarred centers (~ 2.1 Gyr). The 16th–84th percentile ranges for t_{dep} in barred and nonbarred centers are 0.3–1.6 and 0.8–3.6 Gyr, respectively. In contrast, all other prescriptions result in <0.2 dex difference between the median t_{dep} of the two types of systems. Such a small difference between barred and nonbarred centers is even true for the B13 prescription, which shows similarly short t_{dep} for all galaxy centers, which generally matches our results. In particular, the MW α_{CO} leads to two completely overlapping t_{dep} distributions, overestimating the overall t_{dep} in barred galaxy centers by a factor of 3–4 if compared to our results. As for the disks, the median of t_{dep} remains consistent at 2–3 Gyr across all four prescriptions, while it is found to be systematically lower in barred galaxies than in nonbarred galaxies by ~ 0.1 dex.

Notably, our prescription reveals short t_{dep} down to $\lesssim 100$ Myr in some barred galaxy centers, which is not seen with other prescriptions. Such a short timescale is supported by recent simulations of galaxy centers, including effects from bar-driven inflows (e.g., Armillotta et al. 2019; Sormani et al. 2020; Moon et al. 2021). In addition, we note that the overall t_{dep} for galaxy centers is similar between our result and B13’s, both suggesting $t_{\text{dep}} \sim 1$ Gyr, which is shorter than the value of ~ 3 Gyr for the disks. This factor of 3 difference between centers and disks is consistent with recent simulations (e.g., Tress et al. 2020a). However, using the MW or Z-based α_{CO} for galaxy centers obscures such a difference and leads to similar t_{dep} across entire galaxies.

4. Discussion

The correlation of α_{CO} with $\sim 100 \text{ pc}$ scale velocity dispersion with only a $\sigma \sim 0.1$ dex scatter (see Section 3.1), contrary to ~ 0.3 dex or larger scatter using Z- and/or Σ_{star} -based prescriptions, shows that velocity dispersion is an excellent observational tracer for α_{CO} variations in star-forming galaxies. The rationale behind such a strong relation may be that Δv directly traces the optical depth changes that are the dominant effect responsible for altering α_{CO} across these galaxies, as it

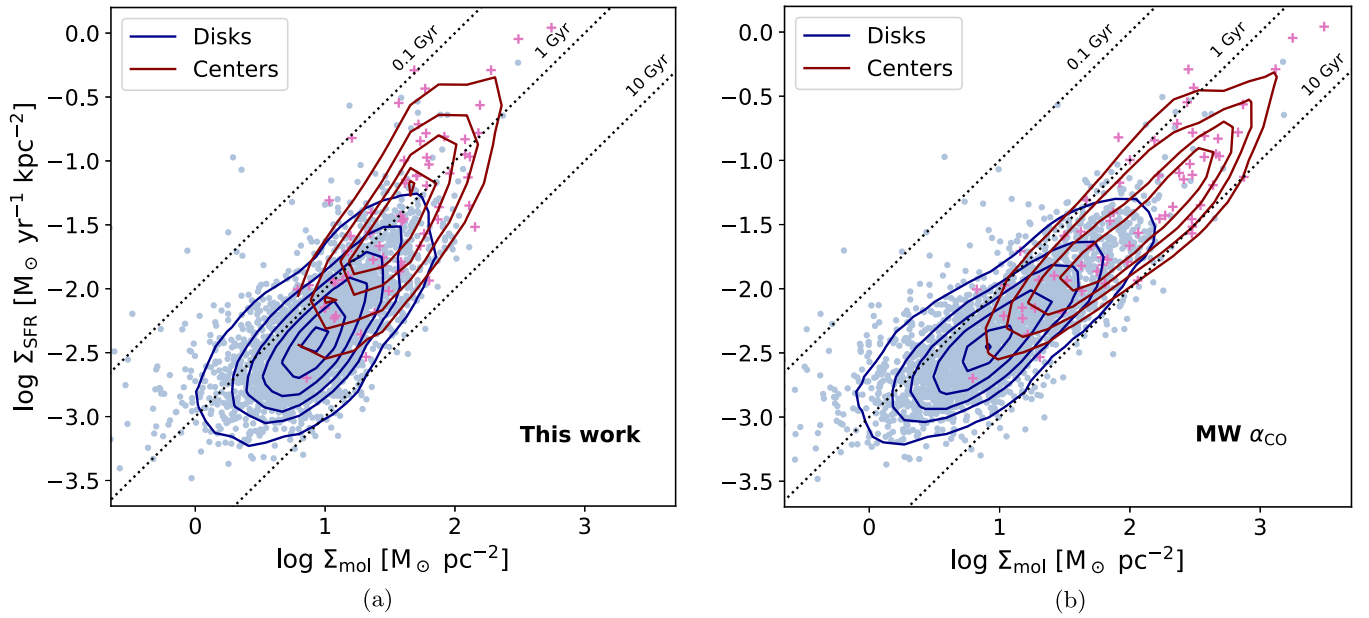


Figure 3. The mKS relation across 65 PHANGS galaxies, where the α_{CO} used to derive Σ_{mol} is based on (a) Equation (2) or (b) the MW value. The thin dotted lines represent constant molecular gas depletion times (t_{dep}) of 0.1, 1, and 10 Gyr. With our α_{CO} prescription, the galaxy centers clearly show a steeper trend than the disks, indicating shorter t_{dep} toward higher Σ_{mol} . Adopting the MW α_{CO} instead results in a roughly constant t_{dep} for both centers and disks.

has been shown that opacity variation is the primary driver of α_{CO} in various galaxy centers (Israel 2020; Teng et al. 2022, T23). However, the effects of CO-dark gas and CO excitation can also be important in explaining α_{CO} variations across the galaxy disks, which have therefore motivated previous α_{CO} prescriptions based on metallicity and/or CO integrated intensity (e.g., Narayanan et al. 2012; Hunt et al. 2015; Amorín et al. 2016; Accurso et al. 2017; Gong et al. 2020).

As discussed in Section 3.2, the correlation of α_{CO} with metallicity (Z') is indirectly included in the dependence with Δv , because both Z' and Δv vary with galactocentric radius and are thus correlated. Furthermore, statistical studies on molecular cloud properties have shown that velocity dispersion also correlates well with molecular gas surface density and the CO integrated intensity across galaxy disks (Heyer et al. 2009; Sun et al. 2020b, 2022; Rosolowsky et al. 2021). Therefore, it is likely that our Δv -based prescription contains opacity variations and metallicity gradients as well as the physics of the α_{CO} - I_{CO} correlation suggested by simulation studies (Narayanan et al. 2012; Gong et al. 2020; Hu et al. 2022). This means that the proposed prescription (Equation (2)) may incorporate more than one piece of physics into a single scaling relation, which could explain why the trend holds across different galactic environments. We also note that metallicity effects on α_{CO} should be more drastic in low-metallicity dwarf galaxies, due to the lack of dust shielding that can prevent CO from dissociation, and thus metallicity variations being included in our Δv -based prescription might only be true in the context of MW-like star-forming disk galaxies as represented by the PHANGS sample.

In Sections 3.3 and 3.4, our prescription (based on the dust α_{CO} measurements) suggests lower α_{CO} in barred galaxy centers, leading to higher SFE than nonbarred centers and the disks. The low α_{CO} and high SFE in barred centers imply that the amount of molecular gas may have been overestimated by previous studies due to inaccurate α_{CO} or the assumption of a

constant SFE. By comparing the derived Σ_{mol} under different α_{CO} assumptions for all galaxies in Table 1, we find that the median Σ_{mol} of barred centers is three times higher than that of nonbarred centers if using an MW-like α_{CO} . On the other hand, our α_{CO} prescription results in only 1.3 times higher Σ_{mol} in barred centers. Therefore, it is likely that the enhanced SFE is a more important factor causing the high SFR observed in barred galaxy centers, compared to an increased amount of molecular gas driven inward by bars.

Recent studies using α_{CO} prescriptions from Narayanan et al. (2012) or B13 also show that barred galaxies tend to have a higher central gas concentration than nonbarred galaxies, although the degree of concentration is not as significant as using a constant α_{CO} (Sakamoto et al. 1999; Sheth et al. 2005; Schinnerer et al. 2006; Kuno et al. 2007). Such accumulation of gas toward the centers can increase the SFR in barred centers, and it is consistent with the theoretical expectation that nonaxisymmetric gravitational potential from bars can induce gas inflows and transport more gas into galaxy centers (e.g., Wada & Habe 1995; Regan & Teuben 2004; Kim et al. 2012; Tress et al. 2020b). Bars thus influence the secular evolution of galaxies by redistributing molecular gas mass and angular momentum (see the review by Kormendy & Kennicutt 2004).

Studies have also shown that if α_{CO} changes were treated properly, starbursts in galaxy centers and variations of SFRs across nearby galaxies would be primarily driven by higher SFE, rather than an increased molecular gas fraction (Leroy et al. 2013; Ellison et al. 2020a, 2020b; den Brok et al. 2023). This is contrary to studies using constant, Z -based, or Σ_{star} -based α_{CO} , which resulted in similar SFE between barred and nonbarred galaxies (e.g., Saintonge et al. 2012; Querejeta et al. 2021; see also Section 3.4). With our proposed α_{CO} prescription, we find enhanced SFE in barred centers, which could originate from variations in molecular gas distribution, density structure, or the dynamical effects of turbulence and shocks powered by stellar feedback (e.g., Kainulainen et al. 2009; Renaud et al. 2012; Liu et al. 2023).

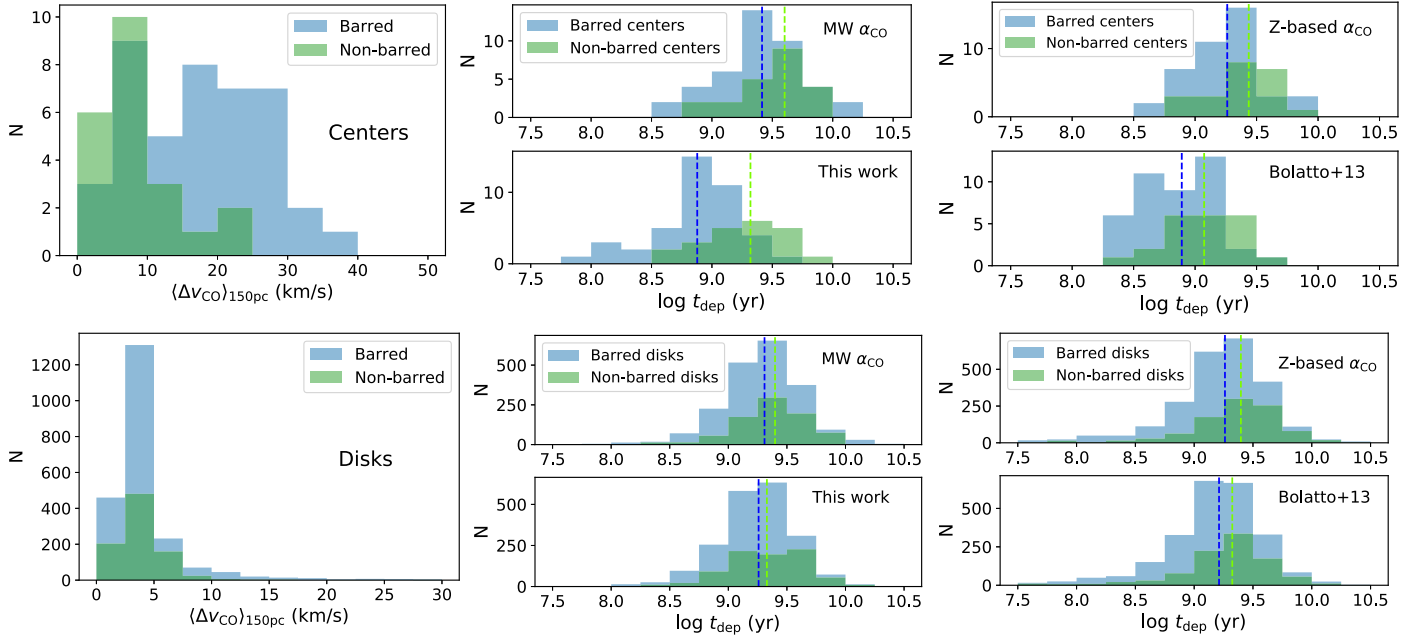


Figure 4. Molecular gas velocity dispersion and the derived depletion time of PHANGS galaxies using four different α_{CO} prescriptions. The upper/lower panels show the center/disk regions. The medians of the barred/nonbarred distributions are indicated by the blue/green dashed lines. Our prescription reveals that barred centers tend to have higher SFE than nonbarred centers due to a generally higher velocity dispersion, but such a trend is easily obscured using other prescriptions. Contrary to the centers, the disk regions show consistent distributions of velocity dispersion and depletion time between barred and nonbarred galaxies, regardless of which prescription is used.

However, these factors driving SFE variations are the same ones that can alter CO emissivity and α_{CO} . Therefore, only with accurate α_{CO} values can we disentangle SFE from α_{CO} and unravel the physical drivers of SFR. Using the latest and best possible measurements of α_{CO} and molecular gas properties across a sample of nearby galaxies, our work lays a foundation for benchmarking α_{CO} calibration in star-forming galaxies (including starbursting galaxy centers) and allows for further investigation into SFE, SFE per cloud freefall time, or other related properties that can improve our knowledge of galaxy evolution.

5. Conclusions

We construct a new α_{CO} prescription applicable to star-forming galaxies, where CO emissivity variations are critical in altering α_{CO} . The prescription is a major step toward the precise calibration of α_{CO} across galaxies, and it reveals unprecedented trends in star formation properties that may have been obscured by previous α_{CO} prescriptions. Our key results are summarized as follows:

1. The strong anticorrelation between measured α_{CO} and CO velocity dispersion (Δv) at ~ 100 pc scales shows that Δv is useful for predicting α_{CO} , and it suggests that CO opacity altered by Δv changes or other correlated properties of the molecular gas across entire galaxies are primary drivers of α_{CO} in star-forming galaxies.
2. The proposed α_{CO} prescription (Equation (2)) is applicable to regions with metallicity above $0.6 Z_{\odot}$ and $\langle \Delta v \rangle_{150 \text{ pc}} \gtrsim 3 \text{ km s}^{-1}$. The expected scatter in α_{CO} is $\sigma \sim 0.1 \text{ dex}$, which is a substantial improvement over existing α_{CO} prescriptions. Our Δv -based prescription has the advantage of connecting directly to the physical causes of α_{CO} change (e.g., CO opacity) as well as

requiring only the CO observations, which are most relevant to tracing molecular gas.

3. With the measured α_{CO} , we find distinctly shorter molecular gas depletion time (t_{dep}) in barred galaxy centers than nonbarred galaxy centers, as well as a generally shorter t_{dep} in galaxy centers than disks. In contrast, assuming a constant MW α_{CO} results in $t_{\text{dep}} \sim 3 \text{ Gyr}$ for all regions, which underestimates the SFE in galaxy centers and also obscures the difference between barred and nonbarred galaxies.
4. Our prescription reveals short t_{dep} down to 100 Myr in barred galaxy centers, with the median t_{dep} ($0.7^{+0.9}_{-0.4} \text{ Gyr}$) being three times shorter than in nonbarred galaxy centers ($2.1^{+1.5}_{-1.3} \text{ Gyr}$). However, all other prescriptions (MW, metallicity-based, and B13) show $< 0.2 \text{ dex}$ difference between the two regions, even if B13 results in an overall shorter t_{dep} for galaxy centers, which aligns better with our results. Thus, the SFE in barred galaxy centers may be underestimated by a factor of three or more in previous studies due to α_{CO} uncertainties.
5. All four prescriptions tested in this work show similar t_{dep} of 2–3 Gyr in the disk regions and nonbarred galaxy centers across the PHANGS sample, which is in good agreement with previous literature (e.g., Leroy et al. 2008; Saintonge et al. 2011; Sun et al. 2023).

Acknowledgments

This work was carried out as part of the PHANGS collaboration. Y.-H.T. and K.S. acknowledge funding support from NRAO Student Observing Support grant SOSPADA-012 and from the National Science Foundation (NSF) under grant No. 2108081. Y.-H.T. also acknowledges support by the Ministry of Education of Taiwan through a Government Scholarship to Study Abroad. J.S. acknowledges support by

the Natural Sciences and Engineering Research Council of Canada (NSERC) through a Canadian Institute for Theoretical Astrophysics (CITA) National Fellowship. K.G. is supported by the Australian Research Council through the Discovery Early Career Researcher Award (DECRA) Fellowship (project number DE220100766) funded by the Australian Government. K.G. is supported by the Australian Research Council Centre of Excellence for All Sky Astrophysics in 3 Dimensions (ASTRO 3D), through project number CE170100013. H.-A.P. acknowledges support by the National Science and Technology Council of Taiwan under grant 110-2112-M-032-020-MY3. M. B. gratefully acknowledges support from the ANID BASAL project FB210003 and from the FONDECYT regular grant 1211000. I.C. thanks the National Science and Technology Council for support through grant 111-2112-M-001-038-MY3 and the Academia Sinica for Investigator Award AS-IA-109-M02. J.C. acknowledges funding from the Belgian Science Policy Office (BELSPO) through the PRODEX project “JWST/MIRI Science exploitation” (C4000142239). M.C. gratefully acknowledges funding from the DFG through an Emmy Noether Research Group (grant number CH2137/1-1). COOL Research DAO is a Decentralized Autonomous Organization supporting research in astrophysics aimed at uncovering our cosmic origins. S.K.S. acknowledges financial support from the German Research Foundation (DFG) via Sino-German research grant SCHI 536/11-1. A.U. acknowledges support from the Spanish grant PID2019-108765GB-I00, funded by MCIN/AEI/10.13039/501100011033. J.D.H. gratefully acknowledges financial support from the Royal Society (University Research Fellowship; URF/R1/221620).

This paper makes use of the following ALMA data: ADS/JAO.ALMA#2012.1.00650.S, ADS/JAO.ALMA#2013.1.00803.S, ADS/JAO.ALMA#2013.1.01161.S, ADS/JAO.ALMA#2015.1.00925.S, ADS/JAO.ALMA#2015.1.00956.S, ADS/JAO.ALMA#2017.1.00392.S, ADS/JAO.ALMA#2017.1.00766.S, ADS/JAO.ALMA#2017.1.00886.L, ADS/JAO.ALMA#2018.1.01321.S, ADS/JAO.ALMA#2018.1.01651.S, and ADS/JAO.ALMA#2018.A.00062.S. ALMA is a partnership of ESO (representing its member states), NSF (USA), and NINS (Japan), together with NRC (Canada), NSC and ASIAA (Taiwan), and KASI (Republic of Korea), in cooperation with the Republic of Chile. The Joint ALMA Observatory is operated by ESO, AUI/NRAO, and NAOJ. The National Radio Astronomy Observatory is a facility of the National Science Foundation operated under cooperative agreement by Associated Universities, Inc. This work is based in part on data products from the Wide-field Infrared Survey Explorer (Wright et al. 2010), which is a joint project of the University of California, Los Angeles, and the Jet Propulsion Laboratory/California Institute of Technology, funded by the National Aeronautics and Space Administration. We acknowledge the usage of the SAO/NASA Astrophysics Data System.

Facilities: ALMA, WISE, Herschel, VLA.

Software: matplotlib (Hunter 2007), numpy (Harris et al. 2020), scipy (Virtanen et al. 2020), astropy (Astropy Collaboration et al. 2013, 2018), ipython (Pérez & Granger 2007).

ORCID iDs

Yu-Hsuan Teng  <https://orcid.org/0000-0003-4209-1599>

I-Da Chiang  <https://orcid.org/0000-0003-2551-7148>

Karin M. Sandstrom  <https://orcid.org/0000-0002-4378-8534>

Jiayi Sun  <https://orcid.org/0000-0003-0378-4667>

Adam K. Leroy  <https://orcid.org/0000-0002-2545-1700>

Alberto D. Bolatto  <https://orcid.org/0000-0002-5480-5686>

Antonio Usero  <https://orcid.org/0000-0003-1242-505X>

Eve C. Ostriker  <https://orcid.org/0000-0002-0509-9113>

Miguel Querejeta  <https://orcid.org/0000-0002-0472-1011>


Jérémy Chastenet  <https://orcid.org/0000-0002-5235-5589>


Frank Bigiel  <https://orcid.org/0000-0003-0166-9745>

Médéric Boquien  <https://orcid.org/0000-0003-0946-6176>

Jakob den Brok  <https://orcid.org/0000-0002-8760-6157>

Yixian Cao  <https://orcid.org/0000-0001-5301-1326>


Mélanie Chevance  <https://orcid.org/0000-0002-5635-5180>

Ryan Chown  <https://orcid.org/0000-0001-8241-7704>

Dario Colombo  <https://orcid.org/0000-0001-6498-2945>

Cosima Eibensteiner  <https://orcid.org/0000-0002-1185-2810>

Simon C. O. Glover  <https://orcid.org/0000-0001-6708-1317>

Kathryn Grasha  <https://orcid.org/0000-0002-3247-5321>

Jonathan D. Henshaw  <https://orcid.org/0000-0001-9656-7682>

María J. Jiménez-Donaire  <https://orcid.org/0000-0002-9165-8080>

Daizhong Liu  <https://orcid.org/0000-0001-9773-7479>

Eric J. Murphy  <https://orcid.org/0000-0001-7089-7325>

Hsi-An Pan  <https://orcid.org/0000-0002-1370-6964>

Sophia K. Stuber  <https://orcid.org/0000-0002-9333-387X>

Thomas G. Williams  <https://orcid.org/0000-0002-0012-2142>

References

- Accurso, G., Saintonge, A., Bisbas, T. G., & Viti, S. 2017, *MNRAS*, **464**, 3315
- Ackermann, M., Ajello, M., Atwood, W. B., et al. 2012, *ApJ*, **750**, 3
- Amorín, R., Muñoz-Tuñón, C., Aguerri, J. A. L., & Planesas, P. 2016, *A&A*, **588**, A23
- Anand, G. S., Lee, J. C., Van Dyk, S. D., et al. 2021, *MNRAS*, **501**, 3621
- Armillotta, L., Krumholz, M. R., Di Teodoro, E. M., & McClure-Griffiths, N. M. 2019, *MNRAS*, **490**, 4401
- Astropy Collaboration, Price-Whelan, A. M., Sipőcz, B. M., et al. 2018, *AJ*, **156**, 123
- Astropy Collaboration, Robitaille, T. P., Tollerud, E. J., et al. 2013, *A&A*, **558**, A33
- Bigiel, F., Leroy, A., Walter, F., et al. 2008, *AJ*, **136**, 2846
- Bolatto, A. D., Wolfire, M., & Leroy, A. K. 2013, *ARA&A*, **51**, 207
- Chiang, I.-D., Sandstrom, K. M., Chastenet, J., et al. 2023, arXiv:2311.00407
- Cicone, C., Severgnini, P., Papadopoulos, P. P., et al. 2018, *ApJ*, **863**, 143
- Cormier, D., Bigiel, F., Jiménez-Donaire, M. J., et al. 2018, *MNRAS*, **475**, 3909
- Davis, T. A., Gensior, J., Bureau, M., et al. 2022, *MNRAS*, **512**, 1522
- De Vis, P., Jones, A., Viaene, S., et al. 2019, *A&A*, **623**, A5
- den Brok, J. S., Bigiel, F., Chastenet, J., et al. 2023, *A&A*, **676**, A93
- Downes, D., & Solomon, P. M. 1998, *ApJ*, **507**, 615
- Draine, B. T. 2011, *Physics of the Interstellar and Intergalactic Medium* (Princeton, NJ: Princeton Univ. Press)
- Ellison, S. L., Lin, L., Thorp, M. D., et al. 2021a, *MNRAS*, **501**, 4777
- Ellison, S. L., Thorp, M. D., Lin, L., et al. 2020a, *MNRAS*, **493**, L39
- Ellison, S. L., Thorp, M. D., Pan, H.-A., et al. 2020b, *MNRAS*, **492**, 6027
- Ellison, S. L., Wong, T., Sánchez, S. F., et al. 2021b, *MNRAS*, **505**, L46
- Esteban, C., Méndez-Delgado, J. E., García-Rojas, J., & Arellano-Córdova, K. Z. 2022, *ApJ*, **931**, 92
- Genzel, R., Tacconi, L. J., Combes, F., et al. 2012, *ApJ*, **746**, 69
- Gong, M., Ostriker, E. C., Kim, C.-G., & Kim, J.-G. 2020, *ApJ*, **903**, 142
- Harris, C. R., Millman, K. J., van der Walt, S. J., et al. 2020, *Natur*, **585**, 357
- Herrero-Illana, R., Privon, G. C., Evans, A. S., et al. 2019, *A&A*, **628**, A71
- Heyer, M., Krawczyk, C., Duval, J., & Jackson, J. M. 2009, *ApJ*, **699**, 1092
- Hu, C.-Y., Schrubba, A., Sternberg, A., & van Dishoeck, E. F. 2022, *ApJ*, **931**, 28

- Hunt, L. K., García-Burillo, S., Casasola, V., et al. 2015, *A&A*, **583**, A114
- Hunter, J. D. 2007, *CSE*, **9**, 90
- Israel, F. P. 1997, *A&A*, **328**, 471
- Israel, F. P. 2020, *A&A*, **635**, A131
- Jiménez-Donaire, M. J., Brown, T., Wilson, C. D., et al. 2023, *A&A*, **671**, A3
- Kainulainen, J., Beuther, H., Henning, T., & Plume, R. 2009, *A&A*, **508**, L35
- Kennicutt, R. C. J. 1998, *ApJ*, **498**, 541
- Kim, W.-T., Seo, W.-Y., Stone, J. M., Yoon, D., & Teuben, P. J. 2012, *ApJ*, **747**, 60
- Koda, J., Hirota, A., Egusa, F., et al. 2023, *ApJ*, **949**, 108
- Kormendy, J., & Kennicutt, R. C. J. 2004, *ARA&A*, **42**, 603
- Kreckel, K., Ho, I. T., Blanc, G. A., et al. 2019, *ApJ*, **887**, 40
- Krieger, N., Ott, J., Beuther, H., et al. 2017, *ApJ*, **850**, 77
- Krumholz, M. R. 2015, arXiv:1511.03457
- Kuno, N., Sato, N., Nakanishi, H., et al. 2007, *PASJ*, **59**, 117
- Lang, P., Meidt, S. E., Rosolowsky, E., et al. 2020, *ApJ*, **897**, 122
- Leroy, A. K., Bolatto, A., Gordon, K., et al. 2011, *ApJ*, **737**, 12
- Leroy, A. K., Schinnerer, E., Hughes, A., et al. 2021, *ApJS*, **257**, 43
- Leroy, A. K., Walter, F., Brinks, E., et al. 2008, *AJ*, **136**, 2782
- Leroy, A. K., Walter, F., Sandstrom, K., et al. 2013, *AJ*, **146**, 19
- Liu, D., Schinnerer, E., Cao, Y., et al. 2023, *ApJL*, **944**, L19
- Lu, A., Boyce, H., Haggard, D., et al. 2022, *MNRAS*, **514**, 5035
- Madden, S. C., Cormier, D., Hony, S., et al. 2020, *A&A*, **643**, A141
- Maeda, F., Egusa, F., Ohta, K., Fujimoto, Y., & Habe, A. 2023, *ApJ*, **943**, 7
- Moon, S., Kim, W.-T., Kim, C.-G., & Ostriker, E. C. 2021, *ApJ*, **914**, 9
- Muraoka, K., Sorai, K., Miyamoto, Y., et al. 2019, *PASJ*, **71**, S15
- Narayanan, D., Krumholz, M. R., Ostriker, E. C., & Hernquist, L. 2012, *MNRAS*, **421**, 3127
- Papadopoulos, P. P., van der Werf, P., Xilouris, E., Isaak, K. G., & Gao, Y. 2012, *ApJ*, **751**, 10
- Pérez, F., & Granger, B. E. 2007, *CSE*, **9**, 21
- Pessa, I., Schinnerer, E., Belfiore, F., et al. 2021, *A&A*, **650**, A134
- Pettini, M., & Pagel, B. E. J. 2004, *MNRAS*, **348**, L59
- Pilyugin, L. S., & Grebel, E. K. 2016, *MNRAS*, **457**, 3678
- Pitts, R. L., & Barnes, P. J. 2021, *ApJS*, **256**, 3
- Querejeta, M., Pety, J., Schruha, A., et al. 2023, *A&A*, **680**, A4
- Querejeta, M., Schinnerer, E., Meidt, S., et al. 2021, *A&A*, **656**, A133
- Ramambason, L., Leboutteiller, V., Madden, S. C., et al. 2023, arXiv:2306.14881
- Regan, M. W., & Teuben, P. J. 2004, *ApJ*, **600**, 595
- Renaud, F., Bournaud, F., Daddi, E., & Weiß, A. 2019, *A&A*, **621**, A104
- Renaud, F., Kraljic, K., & Bournaud, F. 2012, *ApJL*, **760**, L16
- Rosolowsky, E., Hughes, A., Leroy, A. K., et al. 2021, *MNRAS*, **502**, 1218
- Saintonge, A., & Catinella, B. 2022, *ARA&A*, **60**, 319
- Saintonge, A., Kauffmann, G., Wang, J., et al. 2011, *MNRAS*, **415**, 61
- Saintonge, A., Tacconi, L. J., Fabello, S., et al. 2012, *ApJ*, **758**, 73
- Sakamoto, K., Okumura, S. K., Ishizuki, S., & Scoville, N. Z. 1999, *ApJ*, **525**, 691
- Sandstrom, K. M., Leroy, A. K., Walter, F., et al. 2013, *ApJ*, **777**, 5
- Schinnerer, E., Böker, T., Emsellem, E., & Lisenfeld, U. 2006, *ApJ*, **649**, 181
- Schruba, A., Kruijssen, J. M. D., & Leroy, A. K. 2019, *ApJ*, **883**, 2
- Schruba, A., Leroy, A. K., Kruijssen, J. M. D., et al. 2017, *ApJ*, **835**, 278
- Schruba, A., Leroy, A. K., Walter, F., et al. 2011, *AJ*, **142**, 37
- Sharda, P., Menon, S. H., Federrath, C., et al. 2022, *MNRAS*, **509**, 2180
- Sheth, K., Vogel, S. N., Regan, M. W., Thornley, M. D., & Teuben, P. J. 2005, *ApJ*, **632**, 217
- Sliwa, K., Wilson, C. D., Matsushita, S., et al. 2017, *ApJ*, **840**, 8
- Sormani, M. C., Tress, R. G., Glover, S. C. O., et al. 2020, *MNRAS*, **497**, 5024
- Sun, J., Leroy, A. K., Ostriker, E. C., et al. 2020a, *ApJ*, **892**, 148
- Sun, J., Leroy, A. K., Ostriker, E. C., et al. 2023, *ApJL*, **945**, L19
- Sun, J., Leroy, A. K., Rosolowsky, E., et al. 2022, *AJ*, **164**, 43
- Sun, J., Leroy, A. K., Schinnerer, E., et al. 2020b, *ApJL*, **901**, L8
- Teng, Y.-H., Sandstrom, K. M., Sun, J., et al. 2022, *ApJ*, **925**, 72
- Teng, Y.-H., Sandstrom, K. M., Sun, J., et al. 2023, *ApJ*, **950**, 119
- Tress, R. G., Smith, R. J., Sormani, M. C., et al. 2020a, *MNRAS*, **492**, 2973
- Tress, R. G., Sormani, M. C., Glover, S. C. O., et al. 2020b, *MNRAS*, **499**, 4455
- Utomo, D., Bolatto, A. D., Wong, T., et al. 2017, *ApJ*, **849**, 26
- Villanueva, V., Bolatto, A. D., Vogel, S., et al. 2022, *ApJ*, **940**, 176
- Virtanen, P., Gommers, R., Oliphant, T. E., et al. 2020, *NatMe*, **17**, 261
- Wada, K., & Habe, A. 1995, *MNRAS*, **277**, 433
- Williams, T. G., Bureau, M., Davis, T. A., et al. 2023, *MNRAS*, **525**, 4270
- Wilson, C. D., Elmegreen, B. G., Bemis, A., & Brunetti, N. 2019, *ApJ*, **882**, 5
- Wright, E. L., Eisenhardt, P. R. M., Mainzer, A. K., et al. 2010, *AJ*, **140**, 1868
- Yasuda, A., Kuno, N., Sorai, K., et al. 2023, *PASJ*, **75**, 743
- Yuan, Y., Krumholz, M. R., & Burkhardt, B. 2020, *MNRAS*, **498**, 2440